Bi_xTe_y thermoelectric thin films sputtered at room temperature onto moving polymer web: effect of gas pressure on materials properties.

Xudong Tao[a], Kening Wan[b], Bryan W. Stuart[a], Emiliano Bilotti[b], Hazel E. Assender[a].

a: Department of Materials, University of Oxford, Parks Road, OX1 3PH

b: School of Engineering and Materials Science, Queen Mary University of London, Mile End Road, E1 4NS.

Corresponding Author: Hazel E. Assender, hazel.assender@materials.ox.ac.uk

Keywords: Roll-to-roll, Flexible/wearable electronics, Room-temperature sputtering, Bismuth Telluride, Thermoelectrics.

Abstract

Bismuth telluride was deposited onto a dynamic (25 m min^{-1}) polyethylene terephthalate substrate at room temperature using direct current magnetron sputtering in preparation for roll-to-roll manufacture of flexible, low dimensional thermoelectric generators. This study explored the effect of sputtering pressure ranging from 0.03 to 0.6 Pa by adjusting argon flow rate from 50 to 500 sccm. Decreasing argon pressure from 0.6 to 0.03 Pa led to a more stoichiometric target-to-substrate atomic transfer. The coatings, deposited from a Te:Bi = 1.5 atomic ratio target, varied in composition ratio from 1.9 to 3.2, attributed to an obstructive phenomenon of sputtered Bi atoms during transport through the plasma region, under a higher working pressure. In addition, films grown under a lower pressure had wider and flatter grains (the aspect ratio of island width/height decreased from 40 (± 1) at 50 sccm to 10 (± 1) at 500 sccm for a ~80-nm coating), as indicated by images in atomic force microscopy. Electrical resistivity increased with pressure (0.9 ± 0.01 to 8.1 ± 0.2 mΩ•cm in a ~80-nm coating) due to a stronger carrier scattering mechanism and variations in the film composition and band gap. Seebeck coefficient increased with pressure (49.7 ± 0.9 to 84.0 ± 0.5 μV/K) attributable to an increased band gap and a possible energy barrier mechanism at grain boundaries leading to a carrier filtering effect. Power factor of the thermoelectric film was enhanced by decreasing pressure until the argon flow rate was below 250 sccm. The maximum power factor of the Bi-Te thin film achieved was 4.1 (± 0.1) × 10^{-4} W/mK^2 under 0.055 (± 0.004) Pa of argon for a ~55 nm coating, which was achieved here by a real industrial-scale manufacturing process.

1. Introduction

Roll-to-roll (R2R) manufacture of flexible and wearable thermoelectric generators (TEGs) is an important area for study due to an increasing desire for locally generated power to minimise charging and energy storage requirements in applications ranging from body sensors and optical displays to communication devices [1].

In the last few decades, flexible TEGs have been widely studied and explored in a variety of materials including inorganic, organic and inorganic-organic hybrid [2-6]. Bismuth telluride (Bi_2Te_3) is one of the best inorganic thermoelectric (TE) materials for wearable electronics due to its performance at room temperature (bandgap: E_g = 0.2 eV [7]) and a high dimensionless figure of merit, ZT (defined as $ZT = PF \bullet T/\lambda = S^2T/\rho\lambda$, where PF, S, T, ρ, and λ are the power factor, the Seebeck coefficient, the absolute temperature, the electrical resistivity and the thermal conductivity, respectively). Wearable TEGs are often applied as thin films. Unlike bulk TE materials, a thin-film configuration is lightweight, cheap and mechanically flexible [8], and, most importantly, has potential to improve ZT because of the influences of carrier scattering and quantum confinement [9]. In recent publications [10-14], the sputtered bismuth telluride films (Bi-Te) have a PF ranging from 3×10^{-4} to 9.5×10^{-4} W/mK^2.

Fabrication of Bi_2Te_3 thin films by physical vapor deposition and chemical vapor deposition has been extensively reported [15-21]. Because the TE behaviour of Bi_2Te_3 thin film strongly depends on the crystal structure and stoichiometry [7], hot deposition or post-deposition heat treatments have been used to obtain high-quality films [22]. However, to deposit onto flexible polymers, processing temperatures are limited (e.g. to ~67 °C for polyethylene terephthalate (PET), and heating the substrate in high throughput R2R processing in vacuum is a significant engineering challenge. In addition, the desire for high throughput speeds in a R2R process means that thin layers of semiconductor are desirable. Direct current (DC) magnetron sputtering is an attractive technique for R2R processing due to its current dominance in industrial manufacturing [23-25]. Nevertheless, obtaining stoichiometric Bi_2Te_3 thin films by sputtering remains a challenge due to differences between Bi and Te in interatomic dissociation energies and momentum exchange interactions during collisions with the working gas [26]. Given the constraints of film thickness and substrate temperature, an in-depth investigation has been undertaken here to analyse the effect of a critical deposition parameter, the sputtering pressure, on TE properties of Bi-Te film sputtered at room

temperature on a dynamic substrate (at an in-line speed of 25 m min^{-1}) to be compatible with a high-speed R2R manufacturing onto deformable polymer substrates.

Sputtering working pressure can have a remarkable influence on film properties such as crystal structure and grain distribution/size/orientation [27]. Publications investigating pressure on Bi_xTe_y film properties *via* sputtering and applied at room-temperature remain scarce (e.g. [14], for a laboratory-scale radio frequency, RF, sputtering), yet its effect is fundamentally important for modern manufacturing, where low thermal durability substrate materials (such as PET) are required to produce the next generation of low cost flexible TEGs for incorporation into smart wearable technologies. Hence, the objective of this paper is to prepare nm-scale thickness Bi-Te thin films by DC magnetron sputtering in an industrial-scale coater at room temperature and to analyse the intrinsic relationships of working gas pressure with surface features, chemical composition, structural and TE properties of Bi-Te films to progress the understanding of vapour deposition conditions for commercial high-speed R2R manufacturing.

2. Experimental details

2.1 Materials fabrication

Bi_xTe_y thin films were deposited in an Aerre Machine Vacuum R2R webcoater onto flexible PET substrates (~125 μm) at room temperature using a three-inch Bi_2Te_3 target (0.25-inch thickness, indium bonded to 0.125-inch thick Cu backing plate, 99.999% purity, Mi-Net Technology Ltd.) with a target-substrate distance of ~6 cm. A vacuum base pressure of 0.02 Pa was achieved and argon flow rates were varied (50, 100, 250, 350, 450, 500 sccm), equivalent to a working pressure of 2.7 (±0.01), 3.5 (±0.02), 5.5 (±0.4), 9.0 (±0.5), 35.0 (±5), and 60.0 (±10) x 10^{-2} Pa, respectively. In each pressure condition, films with various thickness were obtained by varying the deposition time (1 – 10 mins), and hence the number of passes of the deposition source, and then the films with approximately the same thickness were selected for analysis. Applied target power was maintained as 0.25 kW. PET substrates were attached to the coating drum (circumference 1.8 m) rotated at 25 m min^{-1} during sputtering, requiring multiple rotations for increased thickness. The sputtering source is to one side (horizontally 'directed') of the rotating drum that supports the polymer substrate. A pre-sputtering process without the sample passing under the target was conducted for three mins to clean the target surface.

2.2 Materials Characterisation

Mechanical grade (1196) Si wafers were masked during coating to create a step between coated and uncoated regions, to measure the film thickness using a Veeco DekTak 6M stylus profilometer (n = 5 locations).

The electrical resistivity was calculated using equation (1) by the film thickness and the sheet resistance obtained from an in-house custom four point probe system (at n = 5 locations). Under applied current of 10^{-2}- 10^{-5} A in outer two probes, the voltage was measured in two inner probes *via* an Agilent 34420 A Nano Volt/Micro Ohm meter.

$$\rho = Rs \cdot t = \frac{\pi}{ln2}\left(\frac{V}{I}\right) \cdot t \qquad (1)$$

where ρ is electrical resistivity, Rs is sheet resistance, t is film thickness, V is voltage and I is current.

Roughness and grain size analysis was characterised by atomic force microscopy, AFM (JEOL JSTM-4200D) using tips (NCHV-A, Bruker Ltd.) in tapping mode (at a scan rate of 0.50 lines/s and 512 points/line) over n = 5 independent locations of 0.5 μm × 0.5 μm. Images were processed (flattened and smoothed) using WSxM 5.0 Develop 9.0 software.

The film surface morphology was analysed using a field emission scanning electron microscope (FE-SEM Zeiss Merlin), at 50.0 kX magnification, 5.0 mm working distance, 3.0 kV and 100 pA current probe. The elemental composition was characterised by Energy Dispersive X-Ray Spectroscopy (EDX) in point ID mode over 16 independent points in 4 locations at a working distance and beam voltage of 10.5 mm and 5 kV, respectively, using a (Zeiss Evo) SEM.

X-ray diffraction (XRD), the results of which are given in the appendix, was carried out in a Rigaku Miniflex diffractometer using Cu kα radiation (λ = 0.154 nm) at 30 kV and 10 mA over a range of 2θ between 10° and 80° with a step size of 0.007°. The grain size and lattice strain were calculated from the broadening of XRD peaks using Williamson-Hall method [28] in X'pert Highscore Plus software, with a removal of instrumental broadening by assuming a Gaussian profile and using a polycrystalline Si bulk as a standard reference. XRD was carried out on thicker (1 μm) films to obtain reasonable signal strength from crystalline material. The crystallinity in these room temperature deposited films is low and not significantly textured, and, as we have reported previously [29], is even lower in thinner

films. We have therefore used XRD only as an indication of crystal phases, not trends in crystallinity, phase or orientation with deposition conditions and time.
E_g of films was obtained from a Tauc plot of the absorbance spectra (200 – 3300 nm wavelength) measured using a Cary Varian 5000 UV-visible-NIR spectrometer.

A home-built Hall measurement system (magnet: 0.165 T) with van der Pauw configuration using Keysight Technologies B2901A at room temperature was used to measure the carrier mobility and concentration of three identical square-size specimens (1 cm × 1 cm) with an evaporated silver layer (110 ± 5 nm) at the four corners (0.1 cm × 0.1 cm).

The Seebeck coefficient was measured under a temperature difference of 0.1 – 0.45 K using a Seebeck effect system (MMR Technologies Inc.) at 300 K under nitrogen atmosphere, determined by the ratio of an output voltage generated across the film surface to the temperature difference. An average result was obtained from at least eight measurements. Then, the TE performance of films, PF, was calculated combing effects of ρ and S ($PF = S^2/\rho$).

The sample-to-sample variation was considered in this characterisation. The batch-to-batch variation was assessed in four independent batches deposited under 250 sccm Ar flow, showing variation of 4.4% in film thickness, 3.0% in electrical resistivity and 1.5% in Seebeck coefficient. Batch-to-batch variation has not been included in the error bars in subsequent figures.

3. Results and Discussion

3.1 Coating Thickness

Figure 1 shows an increase in film thickness with sputtering pressure, i.e. an increasing trend of the deposition rate with increasing pressure, as expected. Working gas pressure significantly affects the rate of deposition such that at the lower extremities (5 sccm Ar flow rate at a base pressure of 0.02 Pa in our webcoater, not shown here), there is insufficient ionisation density to sustain a plasma. If the pressure were increased too far, deposition rates would diminish as the density of Bi and Te collisions with Ar gas increases as they travel from the target to the substrate, due to the reduction in the mean free path [30]. However, as in the case here, an intermediate regime exists where the effects of increasing ionisation density and atomic bombardment dominates the reduction in mean free path leading to an increase in deposition rate with pressure [31].

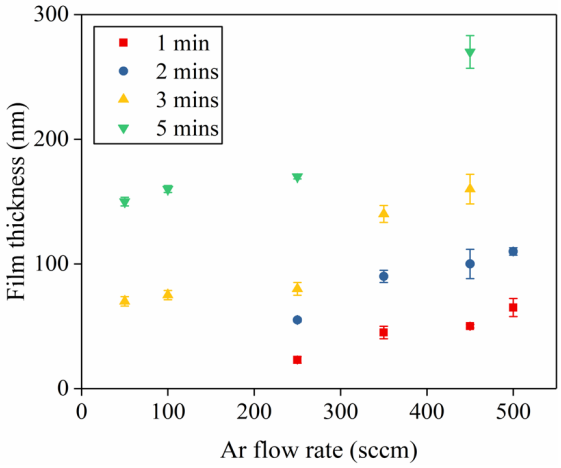

Figure 1. *Film thickness as a function of Ar flow rate after different deposition times of drum rotation. (The error bars are standard deviation from at least five independent area of a single sample). From these data, films of different deposition condition, but similar thickness, could be selectrd for further analysis.*

The materials properties of the polymer (composition and morphology) will depend on the Ar flow rate and the thickness. Thus a broad survey was made of these thin films of thickness about 50 nm to 200 nm thickness. These indicate the overall trends in properties, which inform the conclusions on TEG properties made on films of specific thickness in section 3.4.

3.2 Elemental Composition

The variation of elemental composition with the film thickness and sputtering pressure as measured using EDX is shown in Figure 2. The as-deposited film is Te-rich. We observe an upward trend of Te content with increasing sputtering pressure which could be explained by the effect of: (1) resputtering of the coating; (2) transport of sputtered species in between the target and substrate.

(1) As the pressure increases, the plasma region extends, increasing the plasma density at the film surface. Plasma etching of the film preferentially removes Te because of its higher sputtering yield [32,33]. This factor would cause less Te in the film at a higher pressure, which is inconsistent with our observations. Therefore, the mostly likely explanation is the collisions of sputtered species with the Ar ions and atoms in the plasma.

(2) Because of the larger atomic mass of Bi (209 u) compared to Te (128 u), Te is more diverted from the path to the substrate by any collisions with Ar. With a greater pressure, there is a greater density of Ar species, and both species can be diverted hence increasing the

proportion of Te. This analysis is described by Rossnagel *et al*. [34] as the transition to the diffusive regime, and the same trend has been observed for Bi-Te deposition [14].

The Te-rich Bi-Te film, sputtered at room temperature, is consistent with the observation of sputtering Bi_2Te_3 in [35]. The excess of Te means that probably some Te phase [36] is formed, which has the potential to influence the TE behaviour of as-sputtered film. XRD could have confirmed such phase, however the XRD signal on our very thin films was not detectable. Thicker films were sputtered and measured by XRD, and, as shown in the appendix, only a hint of possible Te phase from the partial broadening of specific peaks.

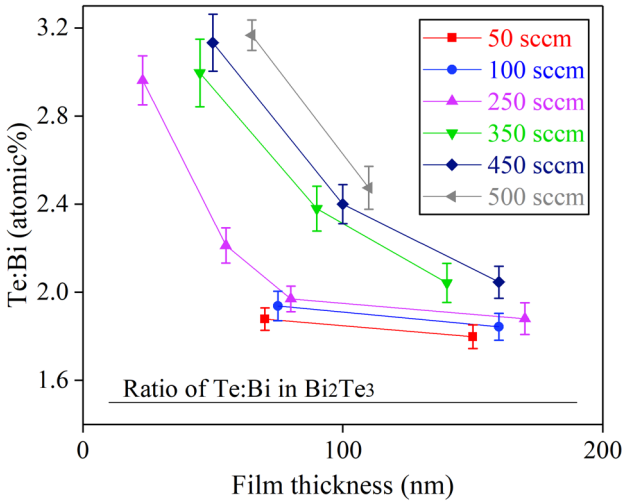

***Figure 2**. Elemental ratio of Te and Bi as a function of film thickness at different pressure conditions. (Lines are to guide the eye. The error bars are standard deviation from at least sixteen independent point measurements in four different locations on a large-area sample)*

3.3 Surface Topography

The film surface topography indicates a granular texture, resulting from the expected island growth mechanism for room temperature sputtering onto polymer. The root mean square roughness (RMSR), and aspect ratio of island width and height are shown in Figure 3 and Figure 4 for a range of thicknesses and pressures. A larger RMSR is observed at a high-pressure condition. Sputtered atoms lose momentum and kinetic energy during the target-to-substrate transport due to collisions with the plasma gas species thus limiting surface atomic diffusion on the substrate [31,37]: such an effect will be greater at high pressure, leading to rougher surfaces. Meanwhile, there is a competitive process that smoothens the film surface caused by the etching effect at high pressure [27]. In our case, the roughness may be dominated by the lower mobility of sputtered atoms on the substrate rather than the etching effect.

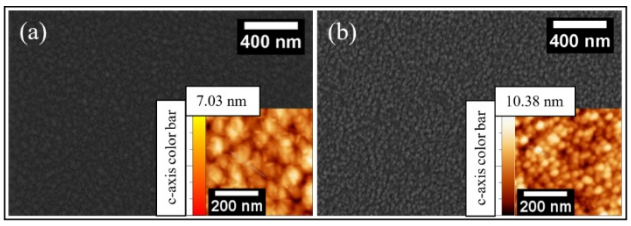

Figure 3. *SEM and AFM images of films grown under (a) 250 sccm and (b) 450 sccm sputter pressure. AFM images: 1-min coating at 250 sccm (23 ± 5 nm) and 450 sccm (50 ± 5 nm); SEM images: 3-min coating at 250 sccm (80 ± 5 nm) and 450 sccm (160 ± 10 nm).*

The sputtering pressure affects grain size, such that the film sputtered under lower pressure exhibits a broader and lower island structure, which can be clearly observed from both AFM and SEM images in Figure 3. To quantify this, an aspect ratio of island width and height (n = 15 islands) from top view of AFM images is analysed (Figure 4b). Although the data from the top view is not an absolute measure of the real size of island, in particular the 'height' is just a measure of the apparent protrusion of the islands, both a decrease in island width and an increase in height are observed as the pressure increases (and the real size of island is expected to follow this trend). For instance, for ~80-nm films, the island width decreases from 104 (±6) nm at 50 sccm to (75 ±3) nm at 450 sccm while the island height increases from 3.1 (±0.2) nm to 8.5 (±0.3) nm. Two reasons are considered to explain the observation of broader/lower island structures under a lower pressure condition:

(1) Different surface diffusion of sputtered atoms on substrates. In the case of a higher pressure, lower adatom mobility (losing kinetic energy travelling through a denser plasma region) kinetically limits the coalescence process, leading to smaller islands formed by nucleation at the initial stage, resulting in smaller overall grains [38].

(2) The morphology tends to coarsen more (to reduce inter-granular interface) at a lower pressure because of more vaporisation/re-deposition/diffusion processes.

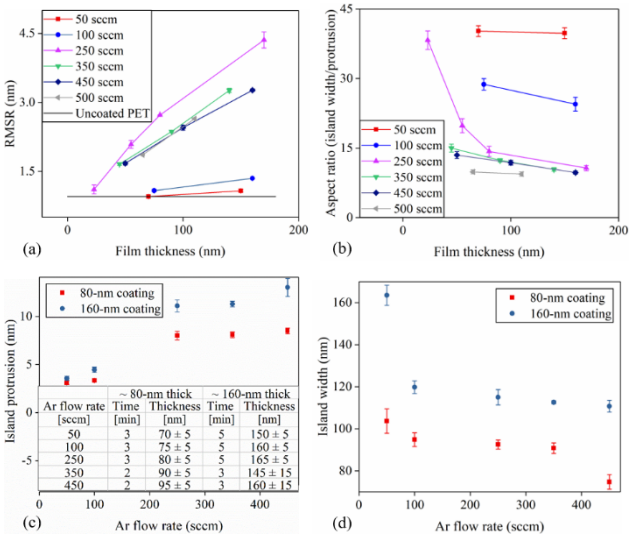

Figure 4. *(a) RMSR of Bi-Te films at different sputtering pressures; (b) Aspect ratio of island width/protrusion form top view of AFM images at various pressure conditions; (c & d) Plots of island width and protrusion vs Ar flow rate for ~80-nm and ~160-nm coatings (inset: the real thickness of samples). The error bars represent standard errors, which are obtained from three AFM images (for RMSR), and at least fifteen independent islands from a large-area sample (for aspect ratio).*

The very thin Bi-Te film sputtered at room temperature is not expected to be highly crystalline as our previous work has shown [29] that the strong peak at (1 0 10) almost disappears for a 100 (±5) nm coating. The grain size has been shown to affect the electrical conductivity of films due to charge scattering at the grain boundary [27]. However, the effect on Seebeck coefficient has not been previously established for the room-temperature sputtered Bi-Te thin film (see section 3.4).

3.4 Thermoelectric Properties

The changes in ρ, S, PF under various sputtering pressures (0.03 - 0.6 Pa) are displayed in Figure 5.

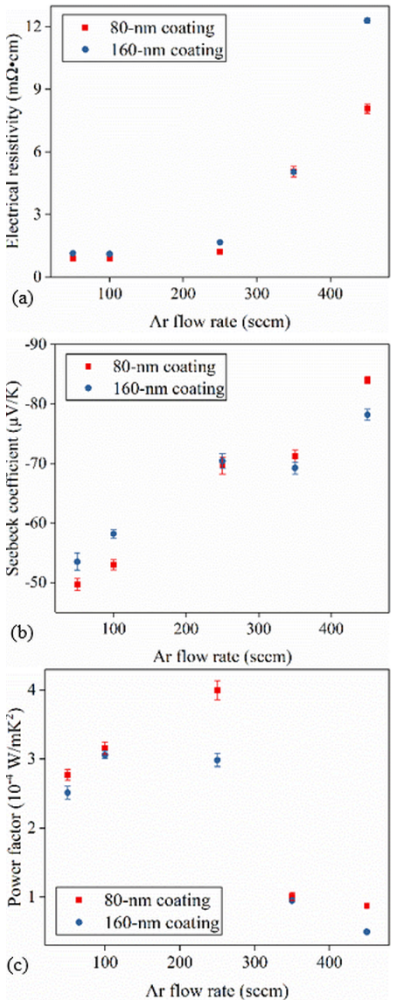

Figure 5. *Plots of (a) ρ, (b) S, (c) PF for 80-nm and 160-nm films grown under various pressures. The error bars are the standard deviation of at least five and eight measurements at different locations for ρ and S, respectively.*

3.4.1 Electrical resistivity

The coatings grown under a lower pressure possess a lower ρ. Hall effect measurements (Figure 6a & b) reveal that the carrier concentration falls with pressure, and after an initial rise between 50 and 100 sccm (possibly due to a more stoichiometric film grown at 50 sccm), the carrier mobility also falls with increasing pressure. Both factors contribute to the observed increase in resistivity. The observed decrease in grain size at higher pressure will decrease the mobility (i.e. the density of grain boundaries on the film affects the carrier scattering effect, see Figure 3). The increased Te content with pressure (see Figure 2) should lead to an increasing trend of carrier concentration if the excess Te occupies the Bi lattice sites and acts as a dopant in Bi_2Te_3, becoming a source of electron donors [39]. However, the observed carrier concentration (from intrinsic carrier generation) appears to decrease with the pressure. The increased E_g, measured from Tauc plot analysis of UV-vis data (see Figure 6c & d), could

be a source of the observed decrease in carrier concentration. The observed increase in E_g could be attributed to the variation of grain size [40] (see Figure 3), stoichiometry [41] (see Figure 2) and crystallinity [42].

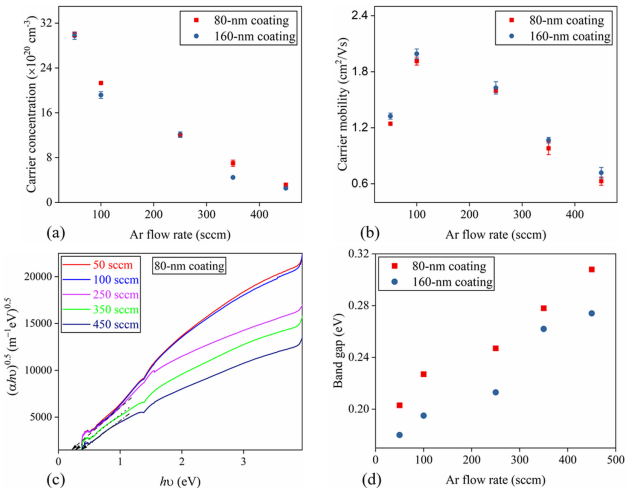

Figure 6. *(a) Variation of carrier concentration and (b) Variation carrier mobility of Bi-Te films as a function of the Ar flow rate i.e. the sputtering pressure (the error bars represent a standard error, obtained from Hall measurements of three identical specimens); (c) Tauc plot of ~80-nm films under different Ar flow rate; (d) Variation of E_g as a function of Ar flow rate.*

3.4.2 Seebeck coefficient

An increasing trend of S is observed as the argon flow rate (i.e. deposition pressure) increases, which could be associated with the decrease in carrier concentration with pressure in Figure 6a (the inverse relationship between S and carrier concentration has been reported by many studies [43-45]). The grain boundary also has effect on S. Under various working pressures, the material forms different grain morphologies (see Figure 3 & **Error! Reference source not found.**) and grain boundaries (e.g. different apparent grain boundary depth as shown by AFM results in Figure 4), which can cause a carrier filtering effect on carrier transport between grains. According to the nature of the grain boundary, energy barriers could be formed either from trapping states [46,47] or other phases [48] present at the grain boundaries.

There are many studies [49-53] reporting other phases (bismuth-telluride-based alloys or bismuth-telluride-oxide-based alloy) involved into the as-prepared Bi-Te based films due to a phase transition from Bi_2Te_3 to bismuth-telluride-based alloys or the chemisorption of oxygen during fabrication. Yuma *et al*. [53] investigated the effect of oxygen content on Bi-Te based films prepared by a hot-pressing method. In their observation, the oxygen mainly distributed

at the grain boundary and the oxygen had an effect on TE behaviours of Bi-Te films. In addition to the sample-fabricating process out of a vacuum, there is a possibility of oxygen existing in Bi-Te films prepared under a vacuum process (e.g. oxygen was observed for a sample prepared by evaporation with a post anneal under vacuum condition [51]). In our case, the sample is very thin/poor crystalline films grown on polymer substrates, hence identifying oxygen phases in the film is not easy. From the results of Te rich (EDX) and poor crystallinity (XRD), we can only deduce that Te-rich (amorphous) phases, at least, are very likely contained in the film (mostly likely at the grain boundary) introducing a carrier filtering effect, which affects TE properties. We observe an increase in S with pressure (Figure 5b): at greater pressure there is greater density of grain boundaries (smaller grains) and increase of apparent grain boundary depth, which, if there is an energy barrier associated with the boundaries may lead to a greater carrier filtering effect.

3.4.3 Power factor

PF ($PF = S^2/\rho$), which is independent of λ, is used here to quantify the TE performance for Bi-Te films. We observe that PF is maximum at moderate pressure, in our case with an Ar flow rate around 250 sccm. As pressure increases above this, the increasing ρ decreases the PF. As the flow decreases below 250 sccm, PF decreases again due to a weak S (high carrier density due to a low E_g, and/or lower effect of any energy barrier carrier filtering effect). In this study, the highest PF for Bi-Te films is 4.1 ($\pm$0.1) $\times$ 10^{-4} W/mK^2 for a 2-min coating (28 passes of the target source at 25 m min^{-1}) under 250 sccm, retaining ~43% of the TE performance but with a much thinner coating (55 $\pm$2 nm) and a faster deposition process, compared with a recently published Bi-Te film of 1.3 μm thickness fabricated in a laboratory-scale RF magnetron sputtering technique (PF = 9.5 $\times$ 10^{-4} W/mK^2, Nuthongkum, *et al*. [14]). They had three variables of pressures and observed that PF increases with pressure. However, due to the wider range of working pressure in this study, we observed that PF increases with pressure before 250 sccm but starts to decrease afterwards due to the greater resistivity, indicating that there is an optimum pressure in sputtering Bi-Te films.

In addition, the majority of laboratory studies focus on RF power because of the inherent poor electrical conductivity of Bi-Te semiconductors causing charging issue on the target during sputtering, while we show that that DC power (at a suitable range) can also be used to sputter Bi_2Te_3 target which makes a step closer to the real R2R process because DC magnetron sputtering (in our case, 20-56 nm/min in a dynamic sputtering $\approx$ 100 – 270

nm/min in a static sputtering) is much faster than RF magnetron sputtering (40 nm/min in static sputtering, [23]) and is often preferred in industrial processes.

4. Conclusion

Variation in Ar-flow rate was experimentally carried out to investigate the effect of processing pressure on the performance of Bi-Te thin films grown on polymer substrates at room temperature using an industrial-scale DC magnetron sputtering technique. At this power (0.25 kW DC), the sputtering rate increased with increasing pressure from around 0.03 to 0.6 Pa. EDX analysis revealed an increasing trend of Te content with pressure thought to be due to a greater obstruction of sputtered Bi atoms as the sputtered species pass through plasma regions as the working pressure increases. The microscopy analysis revealed that grain size was strongly dependent on the sputtering pressure, and bigger/flatter grains tended to form at a lower working pressure. Resistivity of films increased with greater sputtering pressure due to the smaller grain size contributing to more carrier scattering hence lower mobility, and a lower carrier density arising from the increased band gap of the semiconductor. An increasing relationship between the working pressure and Seebeck coefficient was observed, which was attributed to a variation of band gap and a possible energy barrier mechanism at grain boundaries. In our case, in terms of thermoelectric performance, power factor was maximum at an argon flow rate of 250 sccm for Bi_xTe_y films at a 2-min sputtering (~55-nm coating). Herein, we extend a previous study of sputtering pressure of Bi-Te films [14], by applying a wider range of pressure, and found that increasing sputtering pressure cannot unlimitedly improve the film's performance. Most importantly, this study optimises the sputtering parameters (deposition pressure and time) using the higher rate DC sputtering for fabricating very thin Bi-Te films grown onto polymer films at room temperature using an industrial-scale roll-to-roll webcoater system at Oxford, significantly making a step closer to the future high-throughput manufacture of thermoelectric generators in flexible and wearable techniques.

Appendix

To investigate the possible on-Bi_2Te_3 crystal phases in the films, thick samples were generated for XRD study. A 1-μm (± 5 nm) Bi-Te coating (Te : Bi = 1.85 at.%), grown under ~8×10^{-3} Pa, 20 sccm Ar flow rate, 0.1 kW power and an dynamic substrate (attached to a rotating drum at an in-line speed of 11.3 m min^{-1}) in an Edwards Vacuum Coater Auto 306 system, is

scanned to check the phase of Bi-Te film grown at room temperature. In Figure A1, XRD diffraction peaks at 2θ of 27.7°, 38.2°, 40.8°, 57.1° and 62.7° confirm the planes of (0 1 5), (1 0 10), (1 1 0), (2 0 10) and (1 1 15), respectively, as expected in a standard Bi_2Te_3 phase (ICSD #193330). However, the (1 0 10) and (1 1 15) peaks are clearly broadened, which suggest a possibility of overlapping peaks [54] of different phases with a similar crystallographic structure to Bi_2Te_3 (e.g. Te phases in Figure A1). Te phase is considered due to a high Te content from EDX results, as well as a small peak observed at 43.8° which might correspond to (1 1 1) plane of Te. The coexistence of Bi_2Te_3 with Te phases could be due to a local variation in elemental composition [55], resulting from poor adatom diffusion on a cold polymer substrate. Controlling the stoichiometry of the bismuth telluride film is important to achieve the best TE performance [14] because non-stoichiometric precipitates in Bi_2Te_3 films are an important factor for TE behaviour [56,57]. However, Goncalves *et al*. [37] found that the best TE performance was not necessarily associated with a stoichiometric Bi_2Te_3 film. The average crystallite size and lattice strain are 84 (±4) nm and 1.403 (±0.004) %, obtained from Williamson-Hall method from the XRD trace in Figure A1.

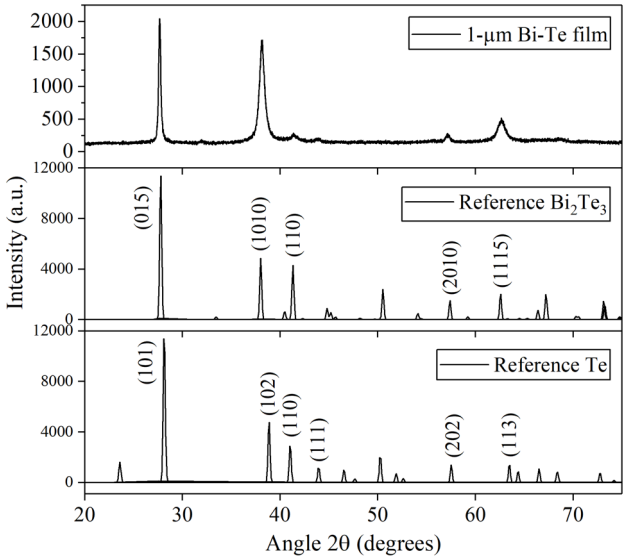

Figure A1. *XRD pattern of 1-µm Bi-Te film, with the references of Te (ICSD #40042) and Bi_2Te_3 (ICSD #193330) powders.*

Acknowledgments

This study was supported by the Engineering and Physical Sciences Research Council [grant number EP/M015173/1] *via* the Wearable and flexible technologies enabled by advanced thin-film manufacture and metrology (WAFT) Collaboration. The authors would like to

acknowledge Oxford Materials Characterisation Services and David Cockayne Centre for Electron Microscopy for equipment access, and would like to especially thank Dr Colin Johnston, Dr Clara Barker, Mrs Nicola Flanagan, Mrs Jennifer Holter, Mrs Radka Chakalova and Mr Richard Turner for technical assistance.

Reference

[1] G. C. Glatzmaier, J. Rea, M. L. Olsen, C. Oshman, C. Hardin, J. Alleman, J. Sharp, R. Weigand, D. Campo, G. Hoeschele, P. A. Parilla, N. P. Siegel, E. S. Toberer, and D. S. Ginley, "Solar thermoelectricity via advanced latent heat storage: A cost-effective small-scale CSP application," *AIP Conference Proceedings*, vol. 1850, no. 1, 2017. http://dx.doi.org/10.1063/1.4984362.

[2] A. R. M. Siddique, S. Mahmud, and B. V. Heyst, "A review of the state of the science on wearable thermoelectric power generators (TEGs) and their existing challenges," *Renewable and Sustainable Energy Reviews*, vol. 73, pp. 730-744, 2017. https://doi.org/10.1016/j.rser.2017.01.177.

[3] J. Bahk, H. Fang, K. Yazawa, and A. Shakouri, "Flexible thermoelectric materials and device optimization for wearable energy harvesting," *J. Mater. Chem. C*, vol. 3, no. 4, pp. 1362-1374, 2015. https://doi.org/10.1039/c5tc01644d.

[4] Y. Zhang and S. Park, "Flexible Organic Thermoelectric Materials and Devices for Wearable Green Energy Harvesting," *Polymers*, vol. 11, no. 5, pp. 909, 2019. https://doi.org/10.3390/polym11050909.

[5] D. Beretta, A. Perego, G. Lanzani, and M. Caironi, "Organic flexible thermoelectric generators: from modeling, a roadmap towards applications," *Sustainable Energy & Fuels*, vol. 1, no. 1, pp. 174-190, 2017. https://doi.org/10.1039/C6SE00028B.

[6] Z. Zheng, P. Fan, J. Luo, G. Liang, H. Ma, X. Zhang, C. Yang, and Y. Q. Fu, "High-performance p-type inorganic-organic hybrid thermoelectric thin films," *Nanoscale*, vol. 10, no. 28, pp. 13511-13519, 2018. https://doi.org/10.1039/C8NR02065E.

[7] Z. H. Zheng, P. Fan, T. B. Chen, Z. K. Cai, P. J. Liu, G. X. Liang, D. P. Zhang, and X. M. Cai, "Optimization in fabricating bismuth telluride thin films by ion beam sputtering deposition," *Thin Solid Films*, vol. 520, no. 16, pp. 5245-5248, 2012. https://doi.org/10.1016/j.tsf.2012.03.086.

[8] X. Chen, W. Dai, T. Wu, W. Luo, J. Yang, W. Jiang, and L. Wang, "Thin Film Thermoelectric Materials: Classification, Characterization, and Potential for Wearable Applications," *Coatings*, vol. 8, no. 7, pp. 244, 2018. https://doi.org/10.3390/coatings8070244.

[9] T. Colpitts, R. Venkatasubramanian, E. Siivola, and B. O'Quinn, "Thin-film thermoelectric devices with high room-temperature figures of merit," *Nature*, vol. 413, no. 6856, pp. 597-602, 2001. http://dx.doi.org/10.1038/35098012.

[10] Z. He, Y. Chen, Z. Zheng, F. Li, G. Liang, J. Luo, and P. Fan, "Enhancement of thermoelectric performance of N-type Bi2Te3 based thin films via in situ annealing during magnetron sputtering," *Ceramics International*, 2020. https://doi.org/10.1016/j.ceramint.2020.02.117.

[11] X. Tao, K. Wan, J. Deru, E. Bilotti, and H. E. Assender, "Thermoelectric behaviour of Bi-Te films on polymer substrates DC-sputtered at room-temperature in moving web deposition," *Surface & Coatings Technology*, vol. 385, pp. 125393, 2020. http://dx.doi.org/10.1016/j.surfcoat.2020.125393.

[12] H. Huang, W. Luan, and S. Tu, "Influence of annealing on thermoelectric properties of bismuth telluride films grown via radio frequency magnetron sputtering," *Thin Solid Films*, vol. 517, no. 13, pp. 3731-3734, 2009. https://doi.org/10.1016/j.tsf.2009.01.015.

[13] D. Kim, E. Byon, G. Lee, and S. Cho, "Effect of deposition temperature on the structural and thermoelectric properties of bismuth telluride thin films grown by co-sputtering," *Thin Solid Films*, vol. 510, no. 1, pp. 148-153, 2006. https://doi.org/10.1016/j.tsf.2005.12.306.

[14] Pilaipon Nuthongkum, Rachsak Sakdanuphab, Mati Horprathum, and Aparporn Sakulkalavek, "[Bi]:[Te] Control, Structural and Thermoelectric Properties of Flexible Bi^sub x^Te^sub y^ Thin Films Prepared by RF Magnetron Sputtering at Different

Sputtering Pressures," *Journal of Electronic Materials*, vol. 46, no. 11, pp. 6444, 2017. https://doi.org/10.1007/s11664-017-5671-x.

[15] A. Bailini, F. Donati, M. Zamboni, V. Russo, M. Passoni, C. S. Casari, A. Li Bassi, and C. E. Bottani, "Pulsed laser deposition of Bi2Te3 thermoelectric films," *Applied Surface Science*, vol. 254, no. 4, pp. 1249-1254, 2007. https://doi.org/10.1016/j.apsusc.2007.09.039.

[16] A. Boyer and E. Cissé, "Properties of thin film thermoelectric materials: application to sensors using the Seebeck effect," *Materials Science & Engineering B*, vol. 13, no. 2, pp. 103-111, 1992. https://doi.org/10.1016/0921-5107(92)90149-4.

[17] A. Giani, F. Pascal-Delannoy, A. Boyer, A. Foucaran, M. Gschwind, and P. Ancey, "Elaboration of Bi2Te3 by metal organic chemical vapor deposition," *Thin Solid Films*, vol. 303, no. 1, pp. 1-3, 1997. https://doi.org/10.1016/S0040-6090(97)00089-8.

[18] Y. Miyazaki and T. Kajitani, "Preparation of Bi2Te3 films by electrodeposition," *Journal of Crystal Growth*, vol. 229, no. 1-4, pp. 542-546, 2001. https://doi.org/10.1016/S0022-0248(01)01225-8.

[19] F. Vlklein, V. Baier, U. Dillner, and E. Kessler, "Transport properties of flash-evaporated (Bi1-xSbx)2Te3 films I: Optimization of film properties," *Thin Solid Films*, vol. 187, no. 2, pp. 253-262, 1990. https://doi.org/10.1016/0040-6090(90)90047-H.

[20] H. Noro, K. Sato, and H. Kagechika, "The thermoelectric properties and crystallography of Bi-Sb-Te-Se thin films grown by ion beam sputtering," *Journal of Applied Physics*, vol. 73, no. 3, pp. 1252-1260, 1993. https://doi.org/10.1063/1.353266.

[21] Z. Zheng, J. Luo, T. Chen, X. Zhang, G. Liang, and P. Fan, "Using high thermal stability flexible thin film thermoelectric generator at moderate temperature," *Applied Physics Letters*, vol. 112, no. 16, pp. 163901, 2018. http://dx.doi.org/10.1063/1.5028390.

[22] C. B. Vining, "An inconvenient truth about thermoelectrics," *Nature Materials*, vol. 8, no. 2, pp. 83-85, 2009. http://dx.doi.org/10.1038/nmat2361.

[23] D. Kim, E. Byon, G. Lee, and S. Cho, "Effect of deposition temperature on the structural and thermoelectric properties of bismuth telluride thin films grown by co-sputtering," *Thin Solid Films*, vol. 510, no. 1, pp. 148-153, 2006. https://doi.org/10.1016/j.tsf.2005.12.306.

[24] D. Bourgault, C. G. Garampon, N. Caillault, L. Carbone, and J. A. Aymami, "Thermoelectric properties of n-type Bi2Te2.7Se0.3 and p-type Bi0.5Sb1.5Te3 thin films deposited by direct current magnetron sputtering," *Thin Solid Films*, vol. 516, no. 23, pp. 8579-8583, 2008. https://doi.org/10.1016/j.tsf.2008.06.001.

[25] T. Chen, P. Fan, Z. Zheng, D. Zhang, X. Cai, G. Liang, and Z. Cai, "Influence of Substrate Temperature on Structural and Thermoelectric Properties of Antimony Telluride Thin Films Fabricated by RF and DC Cosputtering," *Journal of Electronic Materials*, vol. 41, no. 4, pp. 679-683, 2012. https://doi.org/10.1007/s11664-011-1896-2.

[26] B. Stuart, M. Gimeno-Fabra, J. Segal, I. Ahmed, and D. M. Grant, "Preferential sputtering in phosphate glass systems for the processing of bioactive coatings," *Thin Solid Films*, vol. 589, pp. 534-542, 2015. https://doi.org/10.1016/j.tsf.2015.05.072.

[27] Luo Bing-Chi, Li Kai, Kang Xiao-Li, Zhang Ji-Qiang, He Yu-Dan, Luo Jiang-Shan, Wu Wei-Dong and Tang Yong-Jian, "Sputtering pressure influence on growth morphology, surface roughness, and electrical resistivity for strong anisotropy beryllium film," , vol. 23, no. 6, pp. 457-461, 2014. https://doi.org/10.1088/1674-1056/23/6/066804.

[28] G. K. Williamson and W. H. Hall, "X-ray line broadening from filed aluminium and wolfram," *Acta Metallurgica*, vol. 1, no. 1, pp. 22-31, 1953.

[29] K. A. Morgan, T. Tang, I. Zeimpekis, A. Ravagli, C. Craig, J. Yao, Z. Feng, D. Yarmolich, C. Barker, H. Assender, and D. W. Hewak, "High-throughput physical vapour deposition flexible thermoelectric generators," *Scientific Reports*, vol. 9, no. 1, pp. 1-9, 2019. https://doi.org/10.1038/s41598-019-41000-y.

[30] Matthew M. Waite, S. Ismat Shah, and David A. Glocker, "Sputtering Sources - The Society of Vacuum Coaters," *50 Years of Vacuum Coating Technology and the growth of the Society of Vacuum Coaters*, no. 15, pp. 12-50, 2007. https://www.svc.org/DigitalLibrary/documents/2010_Spring_MMWaite_SIShah_DAGlocker_p42-50.pdf.

[31] K. Srinivas, M. Manivel Raja, D. V. Sridhara Rao, and S. V. Kamat, "Effect of sputtering pressure and power on composition, surface roughness, microstructure and magnetic properties of as-deposited Co2FeSi thin films," *Thin Solid Films*, vol. 558, pp. 349-355, 2014. https://doi.org/10.1016/j.tsf.2014.02.052.

[32] M. P. Seah, "Pure element sputtering yields using 500–1000 eV argon ions," *Thin Solid Films*, vol. 81, no. 3, pp. 279-287, 1981. https://doi.org/10.1016/0040-6090(81)90490-9.

[33] M. P. Seah, "An accurate semi-empirical equation for sputtering yields, II: for neon, argon and xenon ions," *Nuclear Inst. and Methods in Physics Research, B*, vol. 229, no. 3-4, pp. 348-358, 2005. https://doi.org/10.1016/j.nimb.2004.12.129.

[34] S. M. Rossnagel, I. Yang, and J. J. Cuomo, "Compositional changes during magnetron sputtering of alloys," *Thin Solid Films*, vol. 199, no. 1, pp. 59-69, 1991. http://dx.doi.org/10.1016/0040-6090(91)90052-Y.

[35] K. Singkaselit, A. Sakulkalavek, and R. Sakdanuphab, "Effects of annealing temperature on the structural, mechanical and electrical properties of flexible bismuth telluride thin films prepared by high-pressure RF magnetron sputtering," *Advances in Natural Sciences: Nanoscience and Nanotechnology*, vol. 8, no. 3, pp. 35002, 2017. https://doi.org/10.1088/2043-6254/aa7222.

[36] Y. Zhao, C. Chang, Y. Jiang, A. DaSilva, Y. Sun, H. Wang, Y. Xing, Y. Wang, K. He, X. Ma, Q. Xue, and J. Wang, "Demonstration of surface transport in a hybrid Bi2Se3/Bi2Te3 heterostructure," *Scientific reports*, vol. 3, no. 1, pp. 3060, 2013. https://doi.org/10.1038/srep03060.

[37] L. M. Goncalves, C. Couto, P. Alpuim, A. G. Rolo, F. Völklein, and J. H. Correia, "Optimization of thermoelectric properties on Bi2Te3 thin films deposited by thermal co-evaporation," *Thin Solid Films*, vol. 518, no. 10, pp. 2816-2821, 2010. https://doi.org/10.1016/j.tsf.2009.08.038.

[38] Y. S. Jung, D. W. Lee, and D. Y. Jeon, "Influence of dc magnetron sputtering parameters on surface morphology of indium tin oxide thin films," *Applied Surface Science*, vol. 221, no. 1, pp. 136-142, 2004. https://doi.org/10.1016/S0169-4332(03)00862-6.

[39] S. Cho, Y. Kim, A. DiVenere, G. K. Wong, J. B. Ketterson, and J. R. Meyer, "Antisite defects of Bi2Te3 thin films," *Applied Physics Letters*, vol. 75, no. 10, pp. 1401-1403, 1999. https://doi.org/10.1063/1.124707.

[40] M. Singh, M. Goyal, and K. Devlal, "Size and shape effects on the band gap of semiconductor compound nanomaterials," *Journal of Taibah University for Science*, vol. 12, no. 4, pp. 470-475, 2018. https://doi.org/10.1080/16583655.2018.1473946.

[41] J. Emara, T. Schnier, N. Pourdavoud, T. Riedl, K. Meerholz, and S. Olthof, "Impact of Film Stoichiometry on the Ionization Energy and Electronic Structure of CH3 NH3 PbI3 Perovskites," *Advanced materials (Deerfield Beach, Fla.)*, vol. 28, no. 3, pp. 553, 2016. https://doi.org/10.1002/adma.201503406.

[42] M. Acosta, I. Riech, and E. Martín-Tovar, "Effects of the Argon Pressure on the Optical Band Gap of Zinc Oxide Thin Films Grown by Nonreactive RF Sputtering," *Advances in Condensed Matter Physics*, vol. 2013, pp. 1-6, 2013. http://dx.doi.org/10.1155/2013/970976.

[43] C Wood, "Materials for thermoelectric energy conversion," *Reports on Progress in Physics*, vol. 51, no. 4, pp. 459-539, 1988. https://doi.org/10.1088/0034-4885/51/4/001.

[44] M. Elsheikh, D. Shnawah, M. Sabri, S. Said, M. Hassan, M. Bashir, and M. Mohamad, "A review on thermoelectric renewable energy: Principle parameters that affect their performance," *Renewable & Sustainable Energy Reviews*, vol. 30, pp. 337-355, 2014. https://doi.org/10.1016/j.rser.2013.10.027.

[45] A. V. Dmitriev and I. P. Zvyagin, "Current trends in the physics of thermoelectric materials," *Physics-Uspekhi*, vol. 53, no. 8, pp. 789-803, 2010. https://doi.org/10.3367/UFNe.0180.201008b.0821.

[46] M. Bachmann, M. Czerner, and C. Heiliger, "Ineffectiveness of energy filtering at grain boundaries for thermoelectric materials," *Phys. Rev. B*, vol. 86, no. 115320https://doi.org/10.1103/PhysRevB.86.115320.

[47] D. L. Medlin and G. J. Snyder, "Interfaces in bulk thermoelectric materials," *Current Opinion in Colloid & Interface Science*, vol. 14, no. 4, pp. 226-235, 2009. https://doi.org/10.1016/j.cocis.2009.05.001.

[48] S. I. Kim, K. Ahn, D. Yeon, S. Hwang, H. Kim, S. M. Lee, and K. H. Lee, "Enhancement of Seebeck Coefficient in Bi0.5Sb1.5Te3 with High-Density Tellurium Nanoinclusions," *Applied Physics Express*, vol. 4, no. 9, pp. 091801-3, 2011. https://doi.org/10.1143/APEX.4.091801.

[49] S. Chen, K. F. Cai, F. Y. Li, and S. Shen, "The Effect of Cu Addition on the System Stability and Thermoelectric Properties of Bi2Te3," *Journal of Electronic Materials*, vol. 43, no. 6, pp. 1966-1971, 2014. https://doi.org/10.1007/s11664-013-2928-x.

[50] P. Anandan, M. Omprakash, M. Azhagurajan, M. Arivanandhan, D. Rajan Babu, T. Koyama, and Y. Hayakawa, "Tailoring bismuth telluride nanostructures using a scalable sintering process and their thermoelectric properties," *CrystEngComm*, vol. 16, no. 34, pp. 7956-7962, 2014. https://doi.org/10.1039/c4ce00837e.

[51] J. Kim, J. Choi, J. Bae, M. Kim, and T. Oh, "Thermoelectric Characteristics of n-Type Bi2Te3 and p-Type Sb2Te3 Thin Films Prepared by Co-Evaporation and Annealing for Thermopile Sensor Applications," *Materials Transactions*, vol. 54, no. 4, pp. 618-625, 2013. https://doi.org/10.2320/matertrans.M2013010.

[52] J. M. Schultz, J. P. McHugh, and W. A. Tiller, "Effects of Heavy Deformation and Annealing on the Electrical Properties of Bi2Te3," *Journal of Applied Physics*, vol. 33, no. 8, pp. 2443-2450, 1962. https://doi.org/10.1063/1.1728990.

[53] Y. Horio and A. Inoue, "Effect of Oxygen Content on Thermoelectric Properties of n-Type (Bi,Sb)2(Te,Se)3 Alloys Prepared by Rapid Solidification and Hot-Pressing Techniques," *MATERIALS TRANSACTIONS*, vol. 47, no. 5, pp. 1412-1416, 2006. https://doi.org/10.2320/matertrans.47.1412.

[54] B. Lanson, "Decomposition of Experimental X-ray Diffraction Patterns (Profile Fitting): A Convenient Way to Study Clay Minerals," *Clays and Clay Minerals*, vol. 45, no. 2, pp. 132-146, 1997. https://doi.org/10.1346/CCMN.1997.0450202.

[55] C. Sudarshan, S. Jayakumar, K. Vaideki, and C. Sudakar, "Effect of vacuum annealing on structural, electrical and thermal properties of e-beam evaporated Bi2Te3 thin films," *Thin Solid Films*, vol. 629, pp. 28-38, 2017. https://doi.org/10.1016/j.tsf.2017.03.043.

[56] L. Yucheng, A. J. Minnich, C. Gang, and R. Zhifeng, "Enhancement of Thermoelectric Figure of Merit by a Bulk Nanostructuring Approach," *Advanced Functional Materials*, vol. 20, no. 3, pp. 357-376, 2010. https://doi.org/10.1002/adfm.200901512.

[57] N. Peranio, E. Leister, W. Töllner, O. Eibl, and K. Nielsch, "Stoichiometry Controlled, Single-Crystalline Bi2Te3 Nanowires for Transport in the Basal Plane," *Advanced Functional Materials*, vol. 22, no. 1, pp. 151-156, 2012. https://doi.org/10.1002/adfm.201101273.

List of figure captions

Figure 1. Film thickness as a function of Ar flow rate after different deposition times of drum rotation. (The error bars are standard deviation from at least five independent area of a single sample). From these data, films of different deposition condition, but similar thickness, could be selectrd for further analysis.

Figure 2. Elemental ratio of Te and Bi as a function of film thickness at different pressure conditions. (Lines are to guide the eye. The error bars are standard deviation from at least sixteen independent point measurements in four different locations on a large-area sample)

Figure 3. SEM and AFM images of films grown under (a) 250 sccm and (b) 450 sccm sputter pressure. AFM images: 1-min coating at 250 sccm (23 ± 5 nm) and 450 sccm (50 ± 5 nm); SEM images: 3-min coating at 250 sccm (80 ± 5 nm) and 450 sccm (160 ± 10 nm).

Figure 4. (a) RMSR of Bi-Te films at different sputtering pressures; (b) Aspect ratio of island width/protrusion form top view of AFM images at various pressure conditions; (c & d) Plots of island width and protrusion vs Ar flow rate for ~80-nm and ~160-nm coatings (inset: the real thickness of samples). The error bars represent standard errors, which are obtained from three AFM images (for RMSR), and at least fifteen independent islands from a large-area sample (for aspect ratio).

Figure 5. Plots of (a) ρ, (b) S, (c) PF for 80-nm and 160-nm films grown under various pressures. The error bars are the standard deviation of at least five and eight measurements at different locations for ρ and S, respectively.

Figure 6. (a) Variation of carrier concentration and (b) Variation carrier mobility of Bi-Te films as a function of the Ar flow rate i.e. the sputtering pressure (the error bars represent a standard error, obtained from Hall measurements of three identical specimens); (c) Tauc plot of ~80-nm films under different Ar flow rate; (d) Variation of E_g as a function of Ar flow rate.

Figure A1. XRD pattern of 1-μm Bi-Te film, with the references of Te (ICSD #40042) and Bi2Te3 (ICSD #193330) powders.